



## Supplementary Materials for

### **Radar evidence of subglacial liquid water on Mars**

R. Orosei\*, S. E. Lauro, E. Pettinelli, A. Cicchetti, M. Coradini, B. Cosciotti, F. Di Paolo, E. Flamini, E. Mattei, M. Pajola, F. Soldovieri, M. Cartacci, F. Cassenti, A. Frigeri, S. Giuppi, R. Martufi, A. Masdea, G. Mitri, C. Nenna, R. Noschese, M. Restano, R. Seu

\*Corresponding author. Email: [roberto.oroisei@inaf.it](mailto:roberto.oroisei@inaf.it)

Published 25 July 2018 on *Science* First Release

DOI: [10.1126/science.aar7268](https://doi.org/10.1126/science.aar7268)

#### **This PDF file includes:**

Materials and Methods  
Supplementary Text  
Figs. S1 to S6  
Table S1  
References

## Materials and Methods

### Instrument description

MARSIS is a subsurface radar sounder on the European Space Agency's Mars Express orbiter. It transmits 1 MHz bandwidth pulses centered at 1.8, 3, 4 or 5 MHz, alternating the transmission at two different frequencies. Pulses are 10- $\mu$ s, 250- $\mu$ s chirped waveforms (linear frequency modulation) transmitted through a 40-m dipole antenna with a repetition frequency of 127.7 Hz (36). The radar collects echoes reflected by the surface and by any other dielectric discontinuity present in the subsurface. Longer wavelengths (lower frequencies) have deeper penetration, but pulse frequency must be above the plasma frequency of the Martian ionosphere to reach the surface.

MARSIS acquires data only when the spacecraft altitude is less than 800-1000 km and operates best in the dark (local night) as echoes suffer far less distortion from the ionosphere.

The radar vertical resolution is approximately 210 m in free space after range compression (i.e., the correlation between transmitted and received waveform) and Hanning windowing (reducing the amplitude of side-lobes caused by range compression) (37). In the subsurface, vertical resolution is improved by a factor equal to the square root of the soil permittivity. Horizontal resolution depends on surface roughness, altitude of the satellite and operating frequency. For most Martian areas, MARSIS lateral resolution is about 10-30 km whereas along track resolution is 5-10 km after Synthetic Aperture Radar (SAR) processing (36), which consists of coherent summation of a batch of consecutive pulses after correction for the vertical motion of the spacecraft.

### Operation Mode and Data calibration

Due to spacecraft data transmission rate limitations, MARSIS is typically programmed to perform SAR processing on board (36). Differently, for the present analysis, raw echo data was used. To achieve this, some instrument software parameters had to be modified (38), so that the raw data bypassed the on-board processing and were stored directly in the instrument memory for the subsequent downlink. This new data collection protocol yielded 3200 consecutive echoes, at two different frequencies, over a continuous ground track approximately 100 km long. Data processing on Earth consisted of range compression and geometric calibration to compensate for altitude variations. In our analysis, SAR processing was not performed because of the smoothness of the SPLD in this area, which causes surface echoes to originate solely from the specular direction; in this case, SAR processing would be reduced to a simple moving average of nadir echoes. Moreover, no correction for ionosphere distortion (39) was applied to the data.

The radiation pattern of MARSIS antenna could not be characterized before launching, due to its large size, thus preventing retrieval of absolute transmitted power. The only possible form of calibration is the correction of geometric power fall-off due to altitude variations. According to the radar equation (40), radar echo power decreases as the inverse of the fourth power of distance between the antenna and the target.

Because of the surface smoothness in this area, topographic roughness is well below the MARSIS wavelength (11, 12) and scattering is almost totally coherent. Under these conditions, the size of the MARSIS footprint is well approximated by the first Fresnel zone. The radius of this zone ranges between 3 and 5 km, depending on satellite altitude

(300-800 km) and frequency (37). The power reflected by a flat disk is proportional to the square of its area (41) and the area of the Fresnel circle increases linearly with altitude. Substituting these quantities in the radar equation, it is found that the decrease of echo power is inversely proportional to the square of distance. To correct geometric power fall-off due to altitude variations, surface echo power is thus normalized by the squared altitude of the spacecraft.

#### Data characteristics and normalization

The collected data can be classified into three general categories according to the intensity and variability of the echoes (see Table S1). Almost a third of the radargrams are characterized by a high signal-to-noise ratio and an almost constant surface power along the ground track. Where different orbits overlap, data acquired with the same frequency show consistent values of both surface and subsurface echo power (Fig. S2). The second subset consists of a limited number of radar profiles whose data show sudden drops of surface echo strength, which are not correlated with the noise level nor with subsurface echo power. These variations take place over distances of a few to several kilometers, and do not depend in any obvious way on solar longitude, solar zenith angle or Martian year. Their location and occurrence seem to change with time, as there are instances in which surface echo power decreases seen in one radar profile are not observed in another overlapping one. Their cause remains unclear, but we hypothesize that they result from patches of CO<sub>2</sub> ice of variable thickness (on the order of 10 m), affecting MARSIS surface echoes in a way similar to those collected over the south residual cap (42). The remaining profiles (third subset) are characterized by a lower signal-to-noise ratio, presumably due to the ionosphere which, in this case, reduces both surface and subsurface echo power and causes signal distortion (43).

All these data have been used to retrieve the basal permittivity by normalizing the power echoes with respect to the median of the surface power computed along each radar profile. Such a normalization has been used to: i) check the uniformity of the surface (Fig. S3 panels A, C, and E) and ii) calibrate the subsurface (Fig. S3 panels B, D, and F). The use of the median has minimized the effects caused by local surface echo power fluctuations observed in some data, without altering the spatial variation of the basal reflectivity along the profiles.

#### Electromagnetic propagation model

To simulate MARSIS radar echoes from the surface and the base of the SPLD, a one-dimensional (1-D) electromagnetic plane wave propagation model was used, similar to those presented in (44) and (45). The model uses the recursive formula (46) to compute the global reflection coefficient of a plane parallel stratigraphy at normal incidence as a function of frequency:

$$R_{i-1}(\omega) = \frac{R_{i-1,i}(\omega) + R_i(\omega) \cdot e^{-2jk_i(\omega)L_i}}{1 + R_{i-1,i}(\omega) \cdot R_i(\omega) e^{-2jk_i(\omega)L_i}} \quad (S1)$$

where  $k_i(\omega)$  is the wave number of the  $i$ -th layer,  $L_i$  the thickness of the  $i$ -th layer, and  $R_{i-1,i}(\omega)$  is the reflection coefficient at the boundary between layer  $i-1$  and  $i$ , given by:

$$R_{i-1,i}(\omega) = \frac{\sqrt{\varepsilon_{i-1}(\omega)} - \sqrt{\varepsilon_i(\omega)}}{\sqrt{\varepsilon_{i-1}(\omega)} + \sqrt{\varepsilon_i(\omega)}} \quad (\text{S2})$$

where  $\varepsilon$  is the layer permittivity.

Planum Australe is modelled as a three-layer structure: a semi-infinite layer with the free space permittivity for the space between the spacecraft and the surface, a homogeneous layer representing the SPLD, and another semi-infinite layer for the material beneath the SPLD. The model computes the echo produced by this stratigraphy, when illuminated by a MARSIS radar pulse under a normal incidence, by iterating equation (S1) for every layer in the model stratigraphy and for every frequency in the MARSIS broadband pulse. Both surface and basal echo power (intensity of the reflected waves) are extracted from the simulated signal and their ratio computed.

#### Dielectric model of the SPLD

The SPLD are represented as a single homogeneous layer consisting of a mixture of H<sub>2</sub>O ice and dust. Internal layering is neglected to simplify computations and reduce the number of model parameters, thus ignoring signal losses due to (possibly multiple) reflections within the SPLD. The effect of CO<sub>2</sub> ice is accounted for separately, simulating the radar response of the overall deposit when layers of CO<sub>2</sub> ice of variable thickness are located at the top or the base of the SPLD (see Supplementary Text below). The permittivity of water ice is computed according to (47), while that of CO<sub>2</sub> ice is taken from (48). Dust within the SPLD is assumed to have a complex permittivity of  $8.8+0.017i$ , typical of basaltic rocks constituting the surface of Mars (44). The permittivity of a mixture of materials is computed by using the Maxwell-Garnett dielectric mixing model (49).

The loss tangent of H<sub>2</sub>O ice is strongly dependent on temperature at MARSIS frequencies (47). A value of 160 K is used to represent the mean annual surface temperature of the SPLD (1), while temperature at the bottom of the SPLD is varied between 170 K and 270 K to account for uncertainties in the Martian geothermal flux and basal thermal properties. The temperature profile within the SPLD is assumed to be a linear interpolation between surface and basal temperatures. Dust content of the SPLD is assumed to range between 2% and 20%, based on current estimates (15). The permittivity at the base of the SPLD, being an unknown parameter, is varied between 3, a value typical of dry porous materials, and 100, which is above that of pure liquid water and is indicative of brines (50).

The baseline model of the radar response of the SPLD consists of an H<sub>2</sub>O ice layer, as thick as the one observed in radargrams over the bright reflector (Fig. 2), containing variable amounts of dust and having variable basal temperature and permittivity. The model produces a set of curves expressing the relation between the normalized basal echo power and the basal permittivity for this ample parameter space. These are used to determine the distribution of the basal permittivity (inside and outside the bright area), by

weighting each admissible value of the permittivity in the chart with the values of the probability distribution of the normalized basal echo power (Fig. 4 and Fig. S4).

## **Supplementary Text**

### Alternative stratigraphic scenarios for the SPLD

CO<sub>2</sub> ice is considered one of the components of the Martian polar caps, and it has been identified in the south residual cap (42, 51). Because it has a lower permittivity compared to the one of water ice (48), CO<sub>2</sub> ice could affect basal echo strength, especially in the case of a resonant CO<sub>2</sub> ice layer (i.e., that produces constructive or destructive signal interference) either at the top (42) or at the base of the SPLD. Occurrence of a CO<sub>2</sub> ice layer in the study area could be hypothesized based on the following evidence:

- Data from both Mars Global Surveyor MOLA (17) and 2001 Mars Odyssey HEND (High Energy Neutron Detector) (16) confirm the presence of a seasonally and locally variable deposit of CO<sub>2</sub> ice less than one meter thick over most of Planum Australe;
- Reflection-free zones (RFZs) observed in SHARAD radargrams (51) are distinct subsurface volumes within which internal layering is only barely discernible or totally absent, in contrast to that observed in the surrounding and underlying terrains. A RFZ has been identified over the study area (covering in fact a much larger region), which is locally about 170m thick. RFZs possess different radar characteristics in different parts of Planum Australe; only a specific type of RFZ in the residual cap could be identified as consisting of CO<sub>2</sub> ice (51).

We are not aware of any direct or indirect observation of layers of CO<sub>2</sub> ice close to or at the base of the SPLD, in agreement with theoretical considerations on the instability of CO<sub>2</sub> ice at large depths (52).

Modelling the effect of a CO<sub>2</sub> layer on radar echo power requires consideration of both its thickness and its depth, which largely increases the model parameter space. The model results have been computed for a CO<sub>2</sub> ice layer that is either at the top or at the bottom of the SPLD, which are hypothesized to consist of H<sub>2</sub>O ice with a dust content fixed at 10% (14), a basal temperature of 205 K (32) and a basal permittivity equal to that of the dust within the SPLD (44). Results related to the CO<sub>2</sub> ice layer at the top of the SPLD are shown in Fig. S5 (A and C) and confirm that the seasonal layer of CO<sub>2</sub> ice (less than 1 m thick) has no effect on surface reflectivity. For a thickness close to a quarter of the transmitted wavelength, i.e., 10-20 m of CO<sub>2</sub> ice, destructive interference between reflections at the top and the bottom of a surface CO<sub>2</sub> ice layer would drastically reduce surface reflectivity (42); however, such a large variation in reflectivity is not observed in the data (Fig. S2). Analysis of a similarly resonant, 10-20 m thick CO<sub>2</sub> ice layer at the bottom of the SPLD resulted in an increase of the normalized basal echo power by about 3 dB (see Fig. S5B and S5D), well below what is observed in the MARSIS data for the bright reflector area.

For a CO<sub>2</sub> ice layer thicker than a few tens of meters, the dominant effect in enhancing subsurface to surface echo power ratio is a weaker attenuation within the CO<sub>2</sub> ice layer. The effect of a thick CO<sub>2</sub> ice layer covering the entire study area, as in the case

of the RFZ mapped by (51), was numerically assessed for a fixed CO<sub>2</sub> ice layer thickness of 200 m. The model was run for the same range of SPLD dust content and basal temperatures considered for the CO<sub>2</sub>-free SPLD model, and results are displayed in Fig. S6. By using these results to derive the value of basal permittivity corresponding to a measured subsurface-to-surface echo power ratio, for all possible combinations of dust content and basal temperature, we still find that estimates within the bright reflector are markedly higher compared to the ones observed elsewhere in the study area. The median values of these permittivity distributions are 14, 16 and 13 (at 3, 4 and 5 MHz) inside the bright reflector and 7, 6 and 6 outside of it. Within the bright reflector, many points have values higher than 15 (more than 50% at 4 MHz), whereas only a few percent of them reach this value outside of bright reflector area (about 4% at 4 MHz).

A final possibility to explain the occurrence of strong basal echoes without a high basal permittivity is that the SPLD are made of very cold, very pure H<sub>2</sub>O ice. Such a possibility seems to be ruled out by estimates of the SPLD density in this area (15) and by the layering observed in MARSIS radargrams (Fig. 2), but it was proposed by (7) for bright basal reflections observed in other parts of Planum Australe. Results of forward electromagnetic simulations based on this assumption are shown in Fig. S6 as a cyan curve. Even in this case, the median value of the normalized basal echo power at 4 MHz corresponds to a basal permittivity of 17, again above the values typical for dry volcanic rocks.

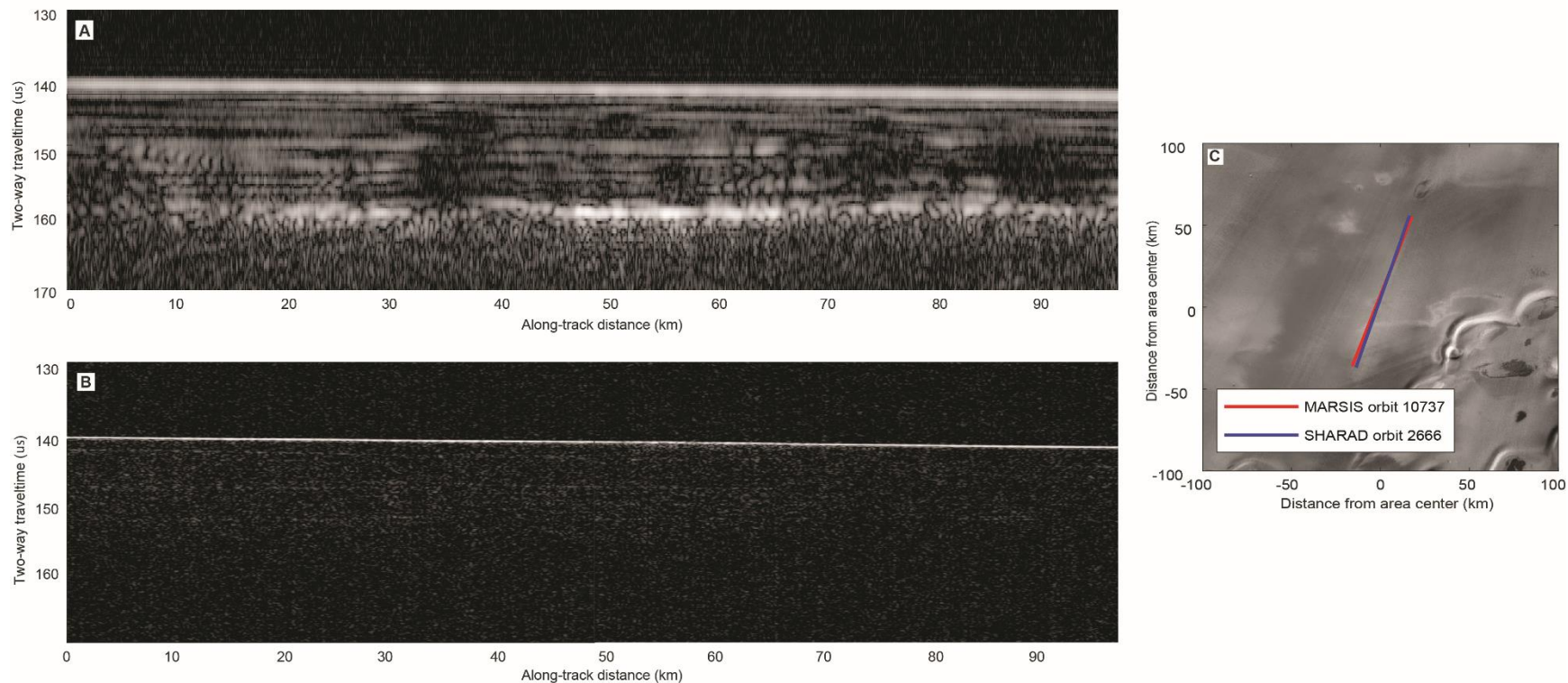


**Fig. S1. Comparison between MARSIS and SHARAD radar data.** (A) MARSIS (orbit 10737) and (B) SHARAD (orbit 2666) radargrams collected in the area with strong basal reflectivity. (C) The ground tracks corresponding to the two radargrams are projected on the same infrared image as Fig. 1B. No basal echo is visible in the SHARAD data, while layering is only faintly discernible amid a diffuse echo attributed to volume scattering in the SPLD between the surface and the basal layer (53), which weakens or masks reflections from its internal layered structure.

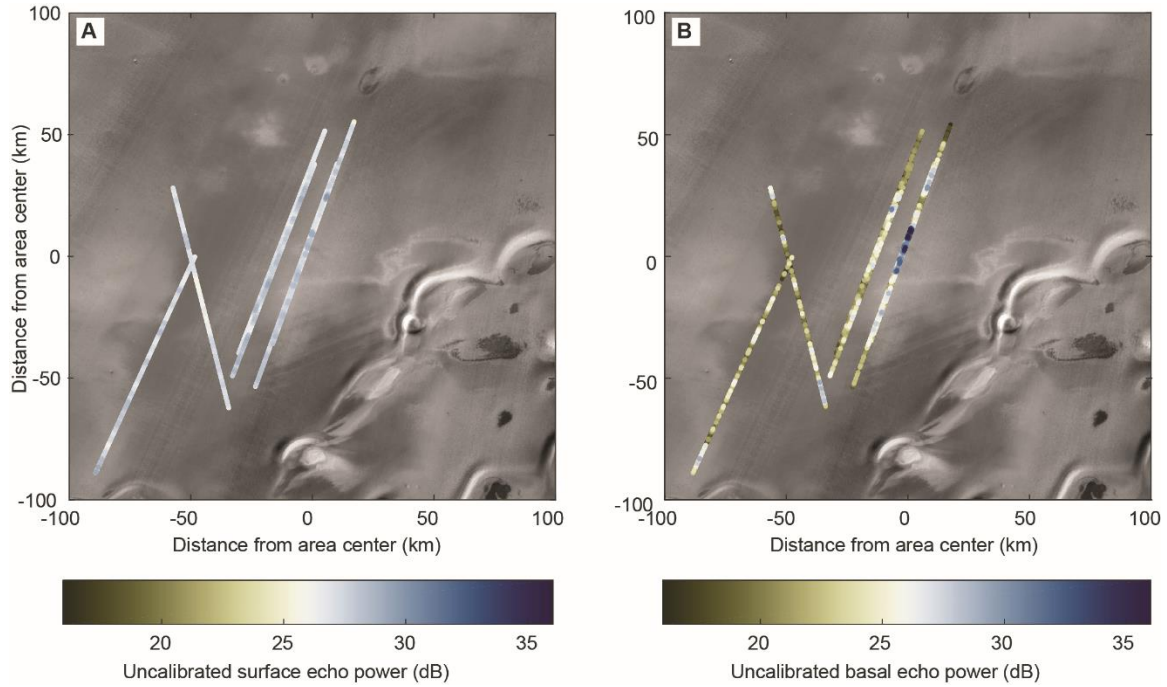


**Fig. S2 Color-coded representation of surface (A) and basal (B) echo power at 4 MHz for MARSIS orbits 10737, 12840, 12847, 12995, 14948 and 14967.** Ground tracks are projected on the same infrared image as Fig. 1B. The data represent the measured echo power after applying only the correction of geometric power fall-off due to altitude variations. The width of the ground tracks has been reduced with respect to the real one to allow the separation of parallel, partially overlapping orbits. Surface echo power fluctuations are limited to a few dB, while there is clustering of strong basal echoes that are consistently observed in different orbits crossing the study area. This indicates that the physical properties of the surface are spatially constant whereas the ones at the base of the SPLD show some lateral variations.



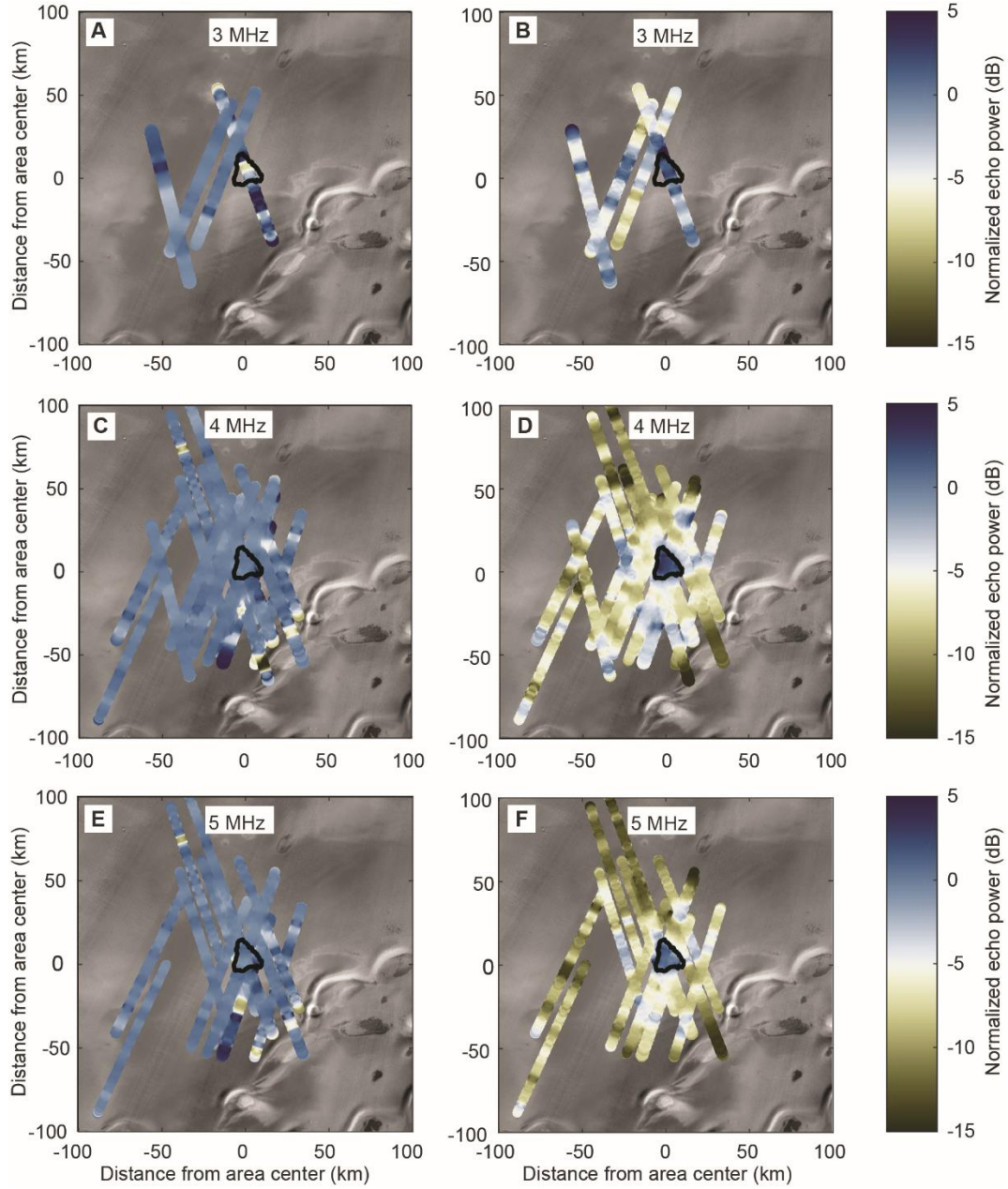


**Fig. S3 Color-coded map of normalized surface (A, C, E) and basal (B, D, F) echo power superimposed on the infrared image in Figure 1B.** Because of the topographic smoothness of the area, the radar footprint size is assumed to correspond to the Fresnel zone of the radar pulse (3-5 km). The mapped value at a given point is the median echo power of all footprints crossing that point. Panels A, C and E show that the surface radar reflectivity is essentially uniform over the area, with only minor, localized and time-varying (seasonal) fluctuations. Panels B, D and F illustrate that the bright basal reflector at the center of the map is visible at all frequencies. The surface reflectivity in the bright area does not exhibit peculiar characteristics compared to the surrounding terrain, except at 3 MHz which we ascribe to limited coverage and low data quality.

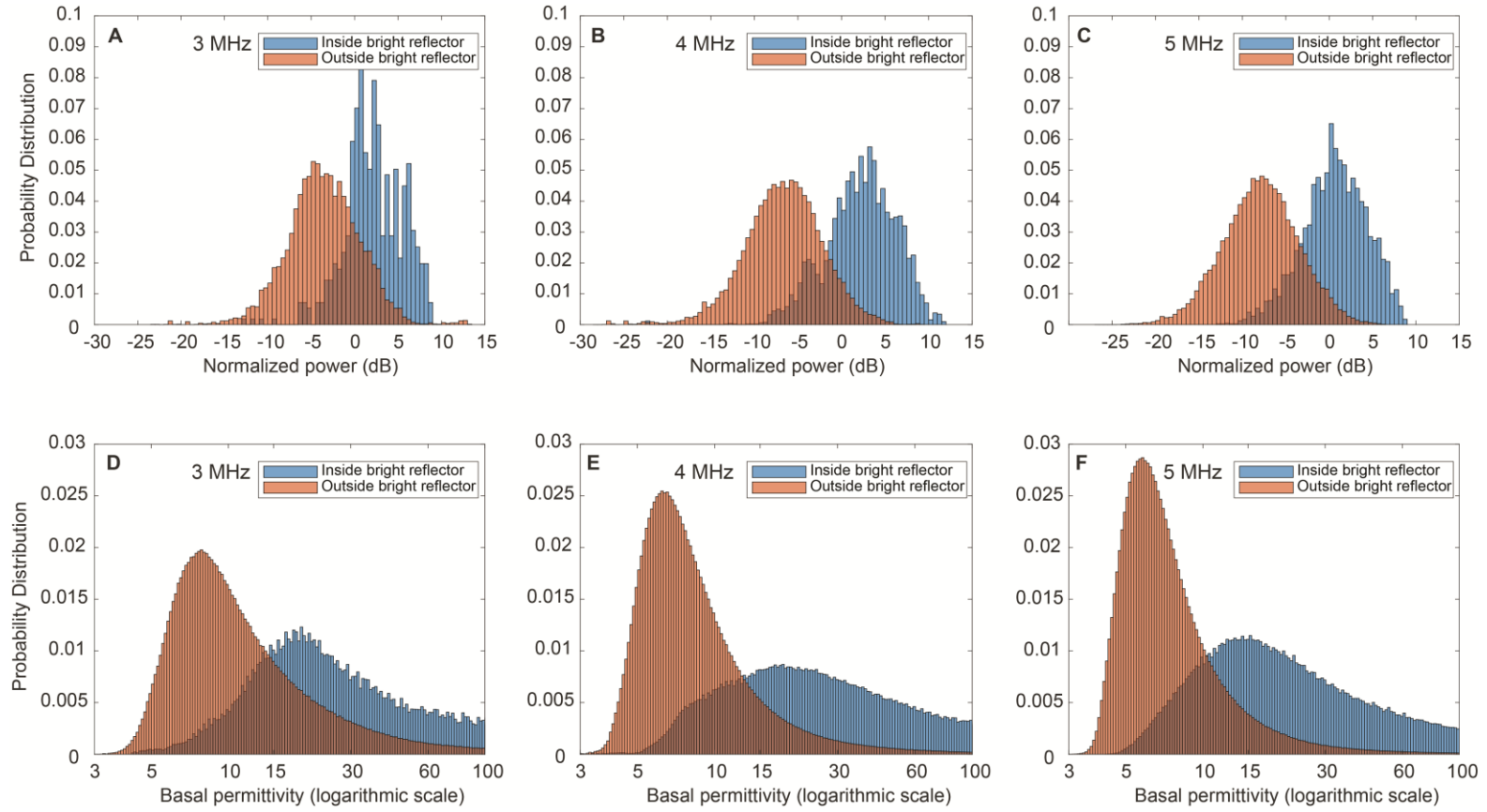


**Fig. S4 Histogram of normalized basal echo power (A-C) and corresponding permittivity values derived from the results of electromagnetic simulations (D-F) at 3, 4 and 5 MHz.** Histograms are computed separately for data points falling inside and outside the bright basal reflector outlined in Fig. 3. The two data sets have clearly distinct statistical properties, and points within the bright reflector produce estimates of basal permittivity larger (median values between 22 and 33) than the values typical of dry volcanic rocks (i.e., 4-15). The long tail of high permittivity values observed in all distributions is caused by the fact that for high values of the basal permittivity, large variations of the permittivity correspond to small variations of basal echo power (Fig. S6). Display is as in Figure 4B-C.

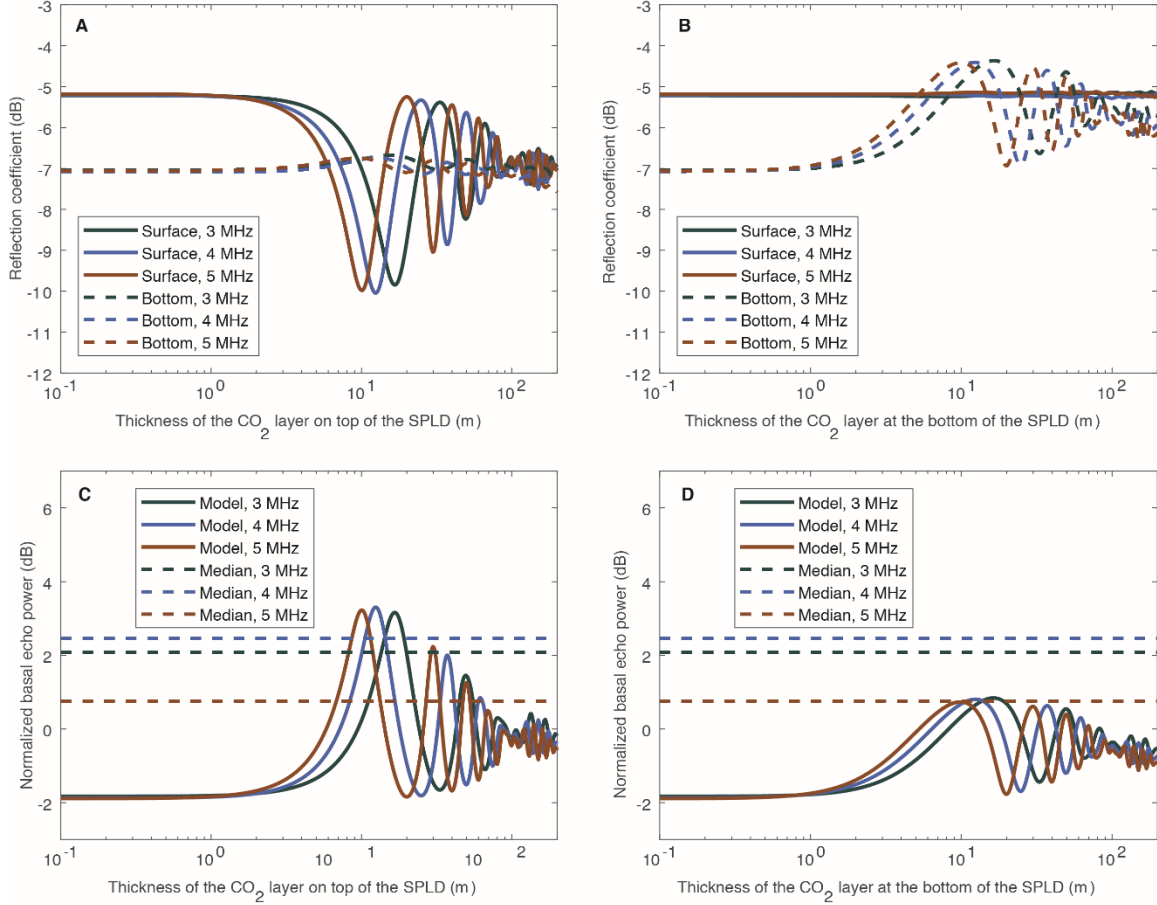


**Fig. S5 Results of electromagnetic propagation simulations for a layer of CO<sub>2</sub> ice of variable thickness at the top and the bottom of the SPLD.** Panels A and C correspond to a CO<sub>2</sub> ice layer overlying the SPLD, while panels B and D are for a CO<sub>2</sub> ice layer beneath it. Panels A and B present values of surface and subsurface reflection coefficients for the three different frequencies employed by MARSIS over the study area. Panels C and D show the corresponding subsurface to surface power ratio compared to the median value observed in MARSIS data inside the bright reflector (dashed lines). The physical properties of the SPLD have been kept fixed (dust content 10%, basal temperature 205 K) for reference. A basal layer of CO<sub>2</sub> ice cannot explain the high values of subsurface to surface power ratio observed within the bright basal reflector. A surface CO<sub>2</sub> ice layer could cause an enhancement of such a ratio similar to the values observed in the bright reflection area, but it would also result in a decrease of surface reflectivity, which is not observed in the data (cf. Fig. S2).

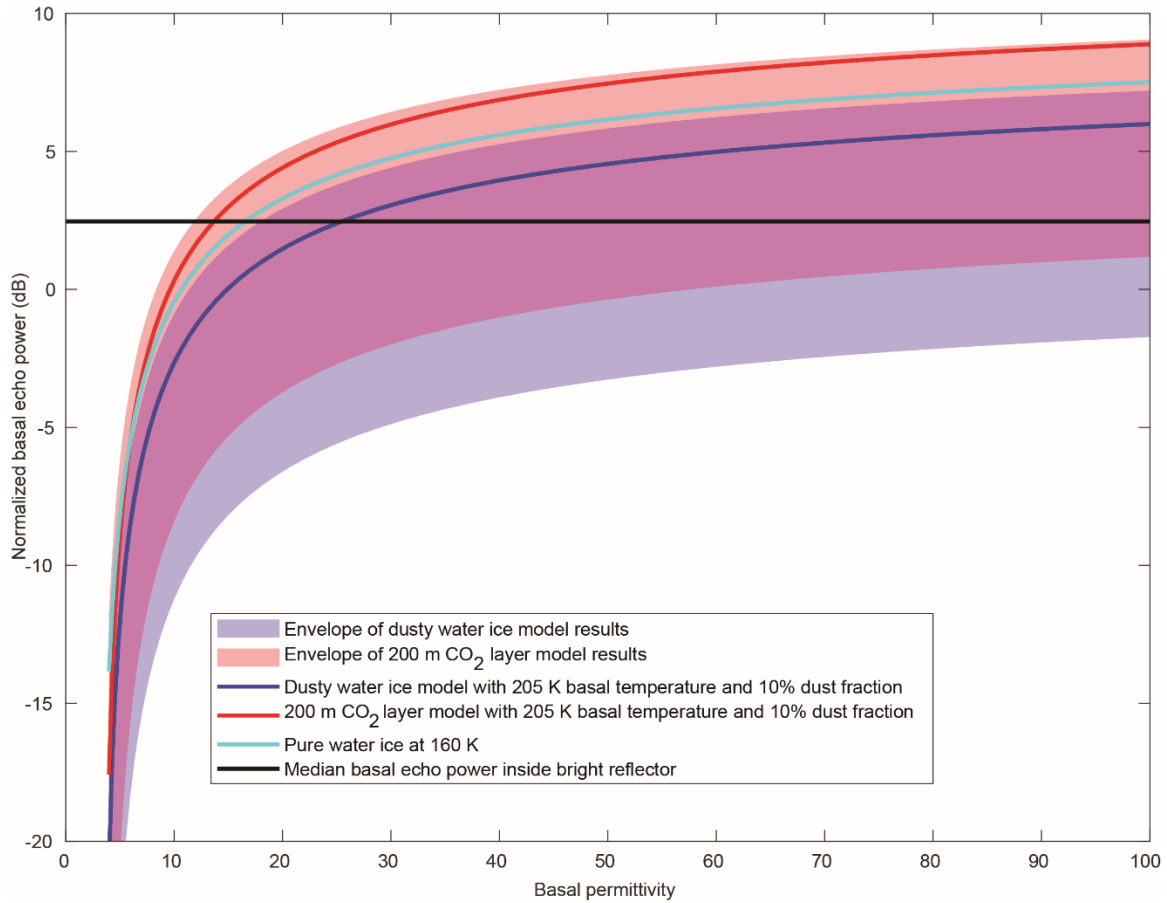


**Fig. S6 Results from numerical simulations of electromagnetic propagation through the SPLD at 4 MHz for the alternative stratigraphic scenarios.** For reference, the blue line is the same as shown in Fig.4. The cyan line corresponds to model results for a pure water ice layer at a uniform temperature of 160 K. The red shaded area encompasses results for the same model SPLD overlain by a 200 m thick layer of CO<sub>2</sub>, while the red curve refers to model results for a 205 K basal temperature and 10% dust content. The envelopes of results for the two sets of models are mostly overlapping, and they both show that positive values of the normalized basal echo power require a basal permittivity of at least 10.

**Table S1. List of MARSIS profiles over the study area.** Profiles taken simultaneously at two frequencies are listed separately for each frequency. The median surface echo power is computed after correction of geometric power fall-off due to altitude variations. The standard deviation of surface echo power provides an indication of the occurrence of surface reflectivity fluctuations. The notes provide a short assessment of data quality. SNR stands for signal-to-noise ratio.

Orbit	Frequency (MHz)	Median surface echo power (dB)	Standard deviation of surface echo power (dB)	Notes
10711	4	29.95	3.90	High SNR, surface echo power fluctuations
10711	5	22.14	4.27	High SNR, surface echo power fluctuations
10737	4	27.95	1.00	High SNR
10737	5	20.20	0.86	High SNR
10961	4	18.80	1.65	Low SNR, surface echo power fluctuations
10961	5	10.44	1.59	Low SNR, surface echo power fluctuations
12685	4	28.98	2.03	High SNR, surface echo power fluctuations
12685	5	20.63	1.68	High SNR, surface echo power fluctuations
12692	4	N/A	N/A	No signal
12692	5	N/A	N/A	No signal
12759	4	18.85	3.11	Low SNR, surface echo power fluctuations
12759	5	13.66	2.92	Low SNR, surface echo power fluctuations
12766	4	23.14	1.30	Medium SNR, surface echo power fluctuations
12766	5	N/A	N/A	Corrupted data
12814	4	27.31	0.74	High SNR, surface echo power fluctuations
12814	5	19.95	0.82	High SNR, surface echo power fluctuations
12840	4	27.80	0.75	High SNR
12840	5	20.21	0.86	High SNR
12847	4	27.70	0.89	High SNR
12847	5	19.88	0.85	High SNR
12895	4	24.23	3.17	Medium SNR, reflectivity fluctuations
12895	5	17.52	2.60	Medium SNR, reflectivity fluctuations
12969	4	27.80	1.19	High SNR, surface echo power

				fluctuations
12969	5	19.88	0.98	High SNR
12995	4	28.19	0.96	High SNR
12995	5	20.512	0.89	High SNR
13002	4	25.74	1.20	Medium SNR
13002	5	18.73	1.07	Medium SNR
13043	4	17.87	1.96	Low SNR, surface echo power fluctuations
13043	5	12.71	1.78	Low SNR, surface echo power fluctuations
13050	4	20.15	0.97	Low SNR
13050	5	14.45	0.84	Low SNR
13069	4	29.24	5.57	High SNR, surface echo power fluctuations
13069	5	22.42	4.58	High SNR, surface echo power fluctuations
14853	4	27.96	1.40	High SNR
14853	5	19.71	1.37	High SNR
14879	4	25.17	0.71	Medium SNR
14879	5	17.46	0.74	Medium SNR
14948	3	23.91	1.79	High SNR
14948	4	27.13	0.74024	High SNR
14967	3	24.63	1.11	High SNR
14967	4	27.18	0.60	High SNR
15055	3	23.50	0.77	High SNR
15055	4	26.46	0.49	High SNR
15110	3	22.34	4.66	Medium SNR, surface echo power fluctuations
15110	4	26.62	3.79	High SNR, surface echo power fluctuations
15136	3	N/A	N/A	Distorted signal
15136	4	31.54	3.92	High SNR, surface echo power fluctuations
15198	3	N/A	N/A	Distorted signal
15198	4	28.23	0.84	High SNR

## References and Notes

1. S. M. Clifford, Polar basal melting on Mars. *J. Geophys. Res.* **92**, 9135–9152 (1987). [doi:10.1029/JB092iB09p09135](https://doi.org/10.1029/JB092iB09p09135)
2. D. W. Ashmore, R. G. Bingham, Antarctic subglacial hydrology: Current knowledge and future challenges. *Antarct. Sci.* **26**, 758–773 (2014). [doi:10.1017/S0954102014000546](https://doi.org/10.1017/S0954102014000546)
3. S. P. Carter, D. D. Blankenship, M. E. Peters, D. A. Young, J. W. Holt, D. L. Morse, Radar-based subglacial lake classification in Antarctica. *Geochem. Geophys. Geosyst.* **8**, 3016 (2007). [doi:10.1029/2006GC001408](https://doi.org/10.1029/2006GC001408)
4. G. Picardi, J. J. Plaut, D. Biccari, O. Bombaci, D. Calabrese, M. Cartacci, A. Cicchetti, S. M. Clifford, P. Edenhofer, W. M. Farrell, C. Federico, A. Frigeri, D. A. Gurnett, T. Hagfors, E. Heggy, A. Herique, R. L. Huff, A. B. Ivanov, W. T. Johnson, R. L. Jordan, D. L. Kirchner, W. Kofman, C. J. Leuschen, E. Nielsen, R. Orosei, E. Pettinelli, R. J. Phillips, D. Plettemeier, A. Safaeinili, R. Seu, E. R. Stofan, G. Vannaroni, T. R. Watters, E. Zampoloni, Radar soundings of the subsurface of Mars. *Science* **310**, 1925–1928 (2005). [doi:10.1126/science.1122165](https://doi.org/10.1126/science.1122165) [Medline](#)
5. Materials and methods are available as supplementary materials.
6. W. M. Farrell, J. J. Plaut, S. A. Cummer, D. A. Gurnett, G. Picardi, T. R. Watters, A. Safaeinili, Is the Martian water table hidden from radar view? *Geophys. Res. Lett.* **36**, L15206 (2009). [doi:10.1029/2009GL038945](https://doi.org/10.1029/2009GL038945)
7. J. J. Plaut, G. Picardi, A. Safaeinili, A. B. Ivanov, S. M. Milkovich, A. Cicchetti, W. Kofman, J. Mouginot, W. M. Farrell, R. J. Phillips, S. M. Clifford, A. Frigeri, R. Orosei, C. Federico, I. P. Williams, D. A. Gurnett, E. Nielsen, T. Hagfors, E. Heggy, E. R. Stofan, D. Plettemeier, T. R. Watters, C. J. Leuschen, P. Edenhofer, Subsurface radar sounding of the south polar layered deposits of Mars. *Science* **316**, 92–95 (2007). [doi:10.1126/science.1139672](https://doi.org/10.1126/science.1139672) [Medline](#)
8. M. Cartacci, A. Frigeri, R. Orosei, E. Pettinelli, paper presented at the American Geophysical Union Fall Meeting, San Francisco, CA, 15 to 19 December 2008.
9. G. K. A. Oswald, S. P. Gogineni, Recovery of subglacial water extent from Greenland radar survey data. *J. Glaciol.* **54**, 94–106 (2008). [doi:10.3189/002214308784409107](https://doi.org/10.3189/002214308784409107)
10. M. J. Siegert, S. Carter, I. Tabacco, S. Popov, D. D. Blankenship, A revised inventory of Antarctic subglacial lakes. *Antarct. Sci.* **17**, 453–460 (2005). [doi:10.1017/S0954102005002889](https://doi.org/10.1017/S0954102005002889)
11. D. E. Smith, M. T. Zuber, H. V. Frey, J. B. Garvin, J. W. Head, D. O. Muhleman, G. H. Pettengill, R. J. Phillips, S. C. Solomon, H. J. Zwally, W. B. Banerdt, T. C. Duxbury, M. P. Golombek, F. G. Lemoine, G. A. Neumann, D. D. Rowlands, O. Aharonson, P. G. Ford, A. B. Ivanov, C. L. Johnson, P. J. McGovern, J. B. Abshire, R. S. Afzal, X. Sun, Mars Orbiter Laser Altimeter: Experiment summary after the first year of global mapping of Mars. *J. Geophys. Res.* **106**, 23689–23722 (2001). [doi:10.1029/2000JE001364](https://doi.org/10.1029/2000JE001364)
12. G. A. Neumann, J. B. Abshire, O. Aharonson, J. B. Garvin, X. Sun, M. T. Zuber, Mars Orbiter Laser Altimeter pulse width measurements and footprint-scale roughness. *Geophys. Res. Lett.* **30**, 1561 (2003). [doi:10.1029/2003GL017048](https://doi.org/10.1029/2003GL017048)



13. C. S. Edwards, K. J. Nowicki, P. R. Christensen, J. Hill, N. Gorelick, K. Murray, Mosaicking of global planetary image datasets: 1. Techniques and data processing for Thermal Emission Imaging System (THEMIS) multi-spectral data. *J. Geophys. Res. Planets* **116**, E10008 (2011). [doi:10.1029/2010JE003755](https://doi.org/10.1029/2010JE003755)
14. M. T. Zuber, R. J. Phillips, J. C. Andrews-Hanna, S. W. Asmar, A. S. Konopliv, F. G. Lemoine, J. J. Plaut, D. E. Smith, S. E. Smrekar, Density of Mars' south polar layered deposits. *Science* **317**, 1718–1719 (2007). [doi:10.1126/science.1146995](https://doi.org/10.1126/science.1146995) [Medline](#)
15. J. Li, J. C. Andrews-Hanna, Y. Sun, R. J. Phillips, J. J. Plaut, M. T. Zuber, Density variations within the south polar layered deposits of Mars. *J. Geophys. Res. Planets* **117**, E04006 (2012).
16. M. L. Litvak, I. G. Mitrofanov, A. S. Kozyrev, A. B. Sanin, V. I. Tretyakov, W. V. Boynton, N. J. Kelly, D. Hamara, R. S. Saunders, Long-term observations of southern winters on Mars: Estimations of column thickness, mass, and volume density of the seasonal CO<sub>2</sub> deposit from HEND/Odyssey data. *J. Geophys. Res. Planets* **112**, E03S13 (2007). [doi:10.1029/2006JE002832](https://doi.org/10.1029/2006JE002832)
17. O. Aharonson, M. Zuber, D. E. Smith, G. A. Neumann, W. C. Feldman, T. H. Prettyman, Depth, distribution, and density of CO<sub>2</sub> deposition on Mars. *J. Geophys. Res. Planets* **109**, E05004 (2004). [doi:10.1029/2003JE002223](https://doi.org/10.1029/2003JE002223)
18. R. Seu, R. J. Phillips, D. Biccari, R. Orosei, A. Masdea, G. Picardi, A. Safaeinili, B. A. Campbell, J. J. Plaut, L. Marinangeli, S. E. Smrekar, D. C. Nunes, SHARAD sounding radar on the Mars Reconnaissance Orbiter. *J. Geophys. Res. Planets* **112**, E05S05 (2007). [doi:10.1029/2006JE002745](https://doi.org/10.1029/2006JE002745)
19. R. Seu, R. J. Phillips, G. Alberti, D. Biccari, F. Bonaventura, M. Bortone, D. Calabrese, B. A. Campbell, M. Cartacci, L. M. Carter, C. Catallo, A. Croce, R. Croci, M. Cutigni, A. Di Placido, S. Dinardo, C. Federico, E. Flamini, F. Fois, A. Frigeri, O. Fuga, E. Giacomoni, Y. Gim, M. Guelfi, J. W. Holt, W. Kofman, C. J. Leuschen, L. Marinangeli, P. Marras, A. Masdea, S. Mattei, R. Mecozzi, S. M. Milkovich, A. Morlupi, J. Mouginot, R. Orosei, C. Papa, T. Paternò, P. Persi del Marmo, E. Pettinelli, G. Pica, G. Picardi, J. J. Plaut, M. Provenziani, N. E. Putzig, F. Russo, A. Safaeinili, G. Salzillo, M. R. Santovito, S. E. Smrekar, B. Tattarletti, D. Vicari, Accumulation and erosion of Mars' south polar layered deposits. *Science* **317**, 1715–1718 (2007). [doi:10.1126/science.1144120](https://doi.org/10.1126/science.1144120) [Medline](#)
20. E. Pettinelli, B. Cosciotti, F. Di Paolo, S. E. Lauro, E. Mattei, R. Orosei, G. Vannaroni, Dielectric properties of Jovian satellite ice analogs for subsurface radar exploration: A review. *Rev. Geophys.* **53**, 593–641 (2015). [doi:10.1002/2014RG000463](https://doi.org/10.1002/2014RG000463)
21. S. E. Lauro, E. Mattei, E. Pettinelli, F. Soldovieri, R. Orosei, M. Cartacci, A. Cicchetti, R. Noschese, S. Giuppi, Permittivity estimation of layers beneath the northern polar layered deposits, Mars. *Geophys. Res. Lett.* **37**, L14201 (2010). [doi:10.1029/2010GL043015](https://doi.org/10.1029/2010GL043015)
22. M. A. Wieczorek, Constraints on the composition of the martian south polar cap from gravity and topography. *Icarus* **196**, 506–517 (2008). [doi:10.1016/j.icarus.2007.10.026](https://doi.org/10.1016/j.icarus.2007.10.026)
23. Z. Zhang, T. Hagfors, E. Nielsen, G. Picardi, A. Mesdea, J. J. Plaut, Dielectric properties of the Martian south polar layered deposits: MARSIS data inversion using Bayesian



- inference and genetic algorithm. *J. Geophys. Res. Planets* **113**, E05004 (2008).  
[doi:10.1029/2007JE002941](https://doi.org/10.1029/2007JE002941)
24. L. M. Carter, B. A. Campbell, J. W. Holt, R. J. Phillips, N. E. Putzig, S. Mattei, R. Seu, C. H. Okubo, A. F. Egan, Dielectric properties of lava flows west of Ascraeus Mons, Mars. *Geophys. Res. Lett.* **36**, L23204 (2009). [doi:10.1029/2009GL041234](https://doi.org/10.1029/2009GL041234)
25. J. Mouginot, A. Pommerol, W. Kofman, P. Beck, B. Schmitt, A. Herique, C. Grima, A. Safaenili, J. J. Plaut, The 3–5 MHz global reflectivity map of Mars by MARSIS/Mars Express: Implications for the current inventory of subsurface H<sub>2</sub>O. *Icarus* **210**, 612–625 (2010). [doi:10.1016/j.icarus.2010.07.003](https://doi.org/10.1016/j.icarus.2010.07.003)
26. Y. Guéguen, V. Palciauskas, *Introduction to the Physics of Rocks* (Princeton Univ. Press, 1994).
27. M. E. Peters, D. D. Blankenship, D. L. Morse, Analysis techniques for coherent airborne radar sounding: Application to West Antarctic ice streams. *J. Geophys. Res. Solid Earth* **110**, B06303 (2005). [doi:10.1029/2004JB003222](https://doi.org/10.1029/2004JB003222)
28. A. A. Maryott, E. R. Smith, Table of Dielectric Constants of Pure Liquids (no. NBS-514, National Bureau of Standards, 1951).
29. M. H. Hecht, S. P. Kounaves, R. C. Quinn, S. J. West, S. M. M. Young, D. W. Ming, D. C. Catling, B. C. Clark, W. V. Boynton, J. Hoffman, L. P. Deflores, K. Gospodinova, J. Kapit, P. H. Smith, Detection of perchlorate and the soluble chemistry of martian soil at the Phoenix lander site. *Science* **325**, 64–67 (2009). [doi:10.1126/science.1172466](https://doi.org/10.1126/science.1172466)  
[Medline](#)
30. D. C. Catling, M. W. Claire, K. J. Zahnle, R. C. Quinn, B. C. Clark, M. H. Hecht, S. Kounaves, Atmospheric origins of perchlorate on Mars and in the Atacama. *J. Geophys. Res. Planets* **115**, E00E11 (2010). [doi:10.1029/2009JE003425](https://doi.org/10.1029/2009JE003425)
31. Y. S. Kim, K. P. Wo, S. Maity, S. K. Atreya, R. I. Kaiser, Radiation-induced formation of chlorine oxides and their potential role in the origin of Martian perchlorates. *J. Am. Chem. Soc.* **135**, 4910–4913 (2013). [doi:10.1021/ja3122922](https://doi.org/10.1021/ja3122922) [Medline](#)
32. D. A. Fisher, M. H. Hecht, S. P. Kounaves, D. C. Catling, A perchlorate brine lubricated deformable bed facilitating flow of the north polar cap of Mars: Possible mechanism for water table recharging. *J. Geophys. Res. Planets* **115**, E00E12 (2010).  
[doi:10.1029/2009JE003405](https://doi.org/10.1029/2009JE003405)
33. J. Lasue, N. Mangold, E. Hauber, S. Clifford, W. Feldman, O. Gasnault, C. Grima, S. Maurice, O. Mosis, Quantitative assessments of the martian hydrosphere. *Space Sci. Rev.* **174**, 155–212 (2013). [doi:10.1007/s11214-012-9946-5](https://doi.org/10.1007/s11214-012-9946-5)
34. C. Grima, F. Costard, W. Kofman, B. Saint-Bézar, A. Servain, F. Rémy, J. Mouginot, A. Herique, R. Seu, Large asymmetric polar scarps on Planum Australe, Mars: Characterization and evolution. *Icarus* **212**, 96–109 (2011).  
[doi:10.1016/j.icarus.2010.12.017](https://doi.org/10.1016/j.icarus.2010.12.017)
35. R. Orosei, A. Cicchetti, Data files and electromagnetic simulation software used in the paper “Radar evidence of subglacial liquid water on Mars”. Zenodo (2018);  
[http://doi.org/10.5281/zenodo.1285179](https://doi.org/10.5281/zenodo.1285179).

36. R. Jordan, G. Picardi, J. Plaut, K. Wheeler, D. Kirchner, A. Safaeinili, W. Johnson, R. Seu, D. Calabrese, E. Zampolini, A. Cicchetti, R. Huff, D. Gurnett, A. Ivanov, W. Kofman, R. Orosei, T. Thompson, P. Edenhofer, O. Bombaci, The Mars express MARSIS sounder instrument. *Planet. Space Sci.* **57**, 1975–1986 (2009). [doi:10.1016/j.pss.2009.09.016](https://doi.org/10.1016/j.pss.2009.09.016)
37. G. Picardi, D. Biccari, R. Seu, J. Plaut, W. T. K. Johnson, R. L. Jordan, A. Safaeinili, D. A. Gurnett, R. Huff, R. Orosei, O. Bombaci, D. Calabrese, E. Zampolini, “MARSIS: Mars advanced radar for subsurface and ionosphere sounding,” in *Mars Express: The Scientific Payload*, A. Wilson, A. Chicarro, Eds. (ESA SP-1240, European Space Agency, 2004).
38. A. Cicchetti, C. Nenna, J. J. Plaut, D. Plettemeier, R. Noschese, M. Cartacci, R. Orosei, Observations of Phobos by the Mars Express radar MARSIS: Description of the detection techniques and preliminary results. *Adv. Space Res.* **60**, 2289–2302 (2017). [doi:10.1016/j.asr.2017.08.013](https://doi.org/10.1016/j.asr.2017.08.013)
39. M. Cartacci, E. Amata, A. Cicchetti, R. Noschese, S. Giuppi, B. Langlais, A. Frigeri, R. Orosei, G. Picardi, Mars ionosphere total electron content analysis from MARSIS subsurface data. *Icarus* **223**, 423–437 (2013). [doi:10.1016/j.icarus.2012.12.011](https://doi.org/10.1016/j.icarus.2012.12.011)
40. J. C. Curlander, R. N. McDonough, *Synthetic Aperture Radar: Systems and Signal Processing* (Wiley, 1991).
41. D. LeVine, The radar cross section of dielectric disks. *IEEE Trans. Antenn. Propag.* **32**, 6–12 (1984). [doi:10.1109/TAP.1984.1143180](https://doi.org/10.1109/TAP.1984.1143180)
42. J. Mouginot, W. Kofman, A. Safaeinili, C. Grima, A. Herique, J. J. Plaut, MARSIS surface reflectivity of the south residual cap of Mars. *Icarus* **201**, 454–459 (2009). [doi:10.1016/j.icarus.2009.01.009](https://doi.org/10.1016/j.icarus.2009.01.009)
43. A. Safaeinili, W. Kofman, J.-F. Nouvel, A. Herique, R. L. Jordan, Impact of Mars ionosphere on orbital radar sounder operation and data processing. *Planet. Space Sci.* **51**, 505–515 (2003). [doi:10.1016/S0032-0633\(03\)00048-5](https://doi.org/10.1016/S0032-0633(03)00048-5)
44. D. C. Nunes, R. J. Phillips, Radar subsurface mapping of the polar layered deposits on Mars. *J. Geophys. Res. Planets* **111**, E06S21 (2006). [doi:10.1029/2005JE002609](https://doi.org/10.1029/2005JE002609)
45. P. Lombardo, A. M. Magenta, E. Pettinelli, Multichannel fusion of subsurface radar images at different resolutions. *IET Radar Sonar Navig.* **147**, 121–133 (2000). [doi:10.1049/ip-rsn:20000196](https://doi.org/10.1049/ip-rsn:20000196)
46. F. T. Ulaby, R. K. Moore, A. K. Fung, *Microwave Remote Sensing Fundamentals and Radiometry*, vol. 1 of *Microwave Remote Sensing: Active and Passive* (Addison-Wesley, 1981).
47. C. Mätzler, “Microwave properties of ice and snow,” in *Solar System Ices*, B. Scmitt, C. de Bergh, M. Festou, Eds. (Springer, 1998), pp. 241–257.
48. E. Pettinelli, G. Vannaroni, A. Cereti, F. Paolucci, G. Della Monica, M. Storini, F. Bella, Frequency and time domain permittivity measurements on solid CO<sub>2</sub> and solid CO<sub>2</sub>-soil mixtures as Martian soil simulants. *J. Geophys. Res. Planets* **108**, 8029 (2003). [doi:10.1029/2002JE001869](https://doi.org/10.1029/2002JE001869)
49. J. C. Maxwell Garnett, Colours in metal glasses and metal films. *Philos. Trans. R. Soc. Lond.* **203**, 385–420 (1904). [doi:10.1098/rsta.1904.0024](https://doi.org/10.1098/rsta.1904.0024)

50. F. T. Ulaby, R. K. Moore, A. K. Fung, *From Theory to Applications*, vol. 3 of *Microwave Remote Sensing: Active and Passive* (Addison-Wesley, 1986).
51. R. J. Phillips, B. J. Davis, K. L. Tanaka, S. Byrne, M. T. Mellon, N. E. Putzig, R. M. Haberle, M. A. Kahre, B. A. Campbell, L. M. Carter, I. B. Smith, J. W. Holt, S. E. Smrekar, D. C. Nunes, J. J. Plaut, A. F. Egan, T. N. Titus, R. Seu, Massive CO<sub>2</sub> ice deposits sequestered in the south polar layered deposits of Mars. *Science* **332**, 838–841 (2011). [doi:10.1126/science.1203091](https://doi.org/10.1126/science.1203091) [Medline](#)
52. A. Dobrovolskis, A. P. Ingersoll, Carbon Dioxide-Water Clathrate as a Reservoir of CO<sub>2</sub> on Mars. *Icarus* **26**, 353–357 (1975). [doi:10.1016/0019-1035\(75\)90178-5](https://doi.org/10.1016/0019-1035(75)90178-5)
53. J. L. Whitten, B. A. Campbell, Lateral continuity of layering in the Mars South Polar Layered Deposits from SHARAD sounding data. *J. Geophys. Res. Planets* 10.1029/2018JE005578 (2018).